Available online at www.sciencedirect.com
ScienceDirect
Trans. Nonferrous Met. Soc. China 31(2021) 178−192

Transactions of
Nonferrous Metals
Society of China
www.tnmsc.cn

Design and characterization of Ti6Al4V/20CoCrMo−highly porous Ti6Al4V biomedical bilayer processed by powder metallurgy

E. MIHALCEA[1], H. J. VERGARA-HERNÁNDEZ[1], O. JIMENEZ[2], L. OLMOS[3], J. CHÁVEZ[4], D. ARTEAGA[5]

1. División de Estudios de Posgrado e Investigación, Tecnológico Nacional de México/ITMorelia,
Av. Tecnológico #1500, Colonia Lomas de Santiaguito, Morelia, C.P. 58120, México;
2. Universidad de Guadalajara, DIP, José Guadalupe Zuno #48, Los Belenes, Zapopan, C. P. 45100, México;
3. INICIT, Universidad Michoacana de San Nicolás de Hidalgo, Fco. J. Mujica S/N, Morelia, C. P. 58060, México;
4. Departamento de Ingeniería Mecánica Eléctrica, CUCEI, Universidad de Guadalajara,
Blvd. Marcelino García Barragán 1421, Olímpica, C. P. 44430 Guadalajara, Jalisco, México;
5. Centro de Geociencias, Universidad Nacional Autónoma de México,
Blvd. Juriquilla No. 3001, Querétaro 76230, México

Received 19 March 2020; accepted 28 November 2020

Abstract: The aim of this work was to develop a Ti6Al4V/20CoCrMo−highly porous Ti6Al4V bilayer for biomedical applications. Conventional powder metallurgy technique, with semi-solid state sintering as consolidation step, was employed to fabricate samples with a compact top layer and a porous bottom layer to better mimic natural bone. The densification behavior of the bilayer specimen was studied by dilatometry and the resulting microstructure was observed by scan electron microscopy (SEM) and computed microtomography (CMT), while the mechanical properties and corrosion resistance were evaluated by compression and potentiodynamic tests, respectively. The results indicate that bilayer samples without cracks were obtained at the interface which has no negative impact on the densification. Permeability values of the highly porous layer were in the lower range of those of human bones. The compression behavior is dictated by the highly porous Ti6Al4V layer. Additionally, the corrosion resistance of Ti6Al4V/20CoCrMo is better than that of Ti6Al4V, which improves the performance of the bilayer sample. This work provides an insight into the important aspects of a bilayer fabrication by powder metallurgy and properties of Ti6Al4V/20CoCrMo−highly porous Ti6Al4V structure, which can potentially benefit the production of customized implants with improved wear performance and increased in vivo lifetime.

Key words: bilayer structure; composites; porosity; sintering; permeability; compression behavior; corrosion

1 Introduction

In the recent years, the demand for bone implants has shown a great increment due to population and average life expectancy growth. Nowadays, most of the materials for bone implants are fabricated from metallic alloys, among them, the Ti alloys, CoCr alloys and the stainless steel are the most used [1−4]. Ti and Ti6Al4V are preferred because they have a lower elastic modulus (*E*) than the other two; however, the *E* of Ti and its alloys is still much higher than that of human bones (0.5−25 MPa), which can lead to the well-known problem of “stress shielding” [4−6]. Therefore, many researchers have devoted to reducing the mechanical properties by making porous materials and the whole range of *E* values has been reproduced [7−13]. A good description of mechanical properties and main techniques to produce porous materials has been reported by TRUEBA et al [14]. An additional advantage of the

---

Corresponding author: L. OLMOS; E-mail: luisra24@gmail.com

DOI: 10.1016/S1003-6326(20)65486-3

porosity is that the porosity allows the circulation of body fluids that contain the nutrients to induce cell growth and bone regeneration [15−19]. Different studies on the pore size have been developed and ITÄLÄ et al [20] suggested that the optimal pore size distribution to promote the bone ingrowth is between 100 and 400 μm. Moreover, the cell ingrowth has been reported to be promoted in the range of 10−50 μm [21]. A more detailed description of the role played by the pore size to promote different cellular activities is given by LOH and CHOONG [22].

On the other hand, when materials are used for high load bearing applications (such as knee or hip replacement), properties like hardness and corrosion resistance are critical for the durability of implants. For such case, Co alloys are preferred because they have better wear and corrosion properties in comparison to Ti alloys [23−25]. In this regard, the most used alloy is CoCrMo, since it combines high hardness and good load bearing capacity under synthetic corporal fluids [23]. Recently, Ti−Co alloys have been developed for dental implants since they have higher hardness than CoCrMo alloys. Also, they can be fabricated at lower temperatures than the CoCrMo, due to a eutectic reaction of Ti and Co at around 1100 °C, depending on the weight percentage of Co [26,27]. More recently, MIHALCEA et al [28] have reported a hardness enhancement in Ti6Al4V/20CoCrMo composites fabricated by semi-solid sintering in comparison to CoCrMo and Ti−Co alloys. Other researchers have directed to improve the hardness and wear behavior of Ti and its alloys by adding ceramic particles, which could generate problems because reinforcing particles can be torn out from the matrix and harm the human body [29−31].

It has been shown that it is difficult to obtain monolithic materials with high hardness and low mechanical properties, thus, the use of multilayer materials might be promising for orthopedic implant applications. Special properties can be obtained by mixing metallic and ceramic components and different microstructures or graded porosity [32]. The properties of these materials highly depend on two things: the kind of material used, and the fabrication method. Two different approaches can be used in order to produce such materials: manufacturing and powder metallurgy. The former (first process) consists in joining two different parts (hot or cold welding using another material or adhesive). This is a very common technique for achieving high-integrity joints between ceramics but, through this process, the high temperature applications of ceramics are often lost. Also, this joint can induce stresses at the interface due to the thermal expansion mismatch of the two materials [33]. The latter (second approach), the most suitable one to produce multilayer materials, is the powder metallurgy route. This technique involves two main steps, green conformation and consolidation by sintering. A complete review of the techniques used to produce multilayer materials has been shown in Ref. [34].

Concerning materials for bone implants applications, a few bilayer component materials have been developed [14,35−40]. Some studies were focused on obtaining a gradient in porosity, either in the radial or in axial direction of the component [14,35−38]; whereas CHÁVEZ et al [39,40] fabricated bilayer components based on Ti6Al4V alloy by reinforcing the top layer with TiN and Ta particles in order to improve the wear and corrosion resistance. They found that co-sintering of layers with different characteristics with similar matrix will lead to a good joint between layers compared to materials that combine metal−ceramic joints.

The main goal of the present work is to develop a bilayer component that has different properties in order to fulfill the characteristics required for bone implants. Thus, an investigation on densification, structural and microstructural evolution during co-sintering of a bilayer component with a highly porous Ti6Al4V layer, and a layer consisting of a composite of Ti6Al4V/20CoCrMo was carried out by means of dilatometry. Because of the eutectic reaction occurring between the Ti and Co at 1120 °C, Ti6Al4V/20CoCrMo was sintered by semi-solid state, generating a higher hardness composite than Ti6Al4V [28]. For comparison reasons, single-layer materials were also fabricated in this study. Microstructure was analyzed by scanning electron microscopy and computed microtomography (CMT). Mechanical properties were evaluated by microhardness and compression tests. Corrosion resistance was evaluated by potentiodynamic polarization tests. Additionally, permeability was evaluated by numerical simulations on the real microstructure, from 3D images.

2 Experimental

2.1 Sample preparation

2.1.1 Initial powders

Three different kinds of powders were used to prepare the samples studied in this work, and spherical prealloyed Ti6Al4V (Fig. 1(a)) and CoCrMo (Fig. 1(b)) powders with a particle size distribution lower than 25 µm, from Raymor, Quebec, Canada and SANDVIK Osprey™, Sweden, respectively were used. Besides, ammonium bicarbonate (NH_4HCO_3) particles (Fig. 1(c)) with irregular shape and size distribution between 100 and 500 µm, furnished by Alfa Aesar, were used to induce large pores.

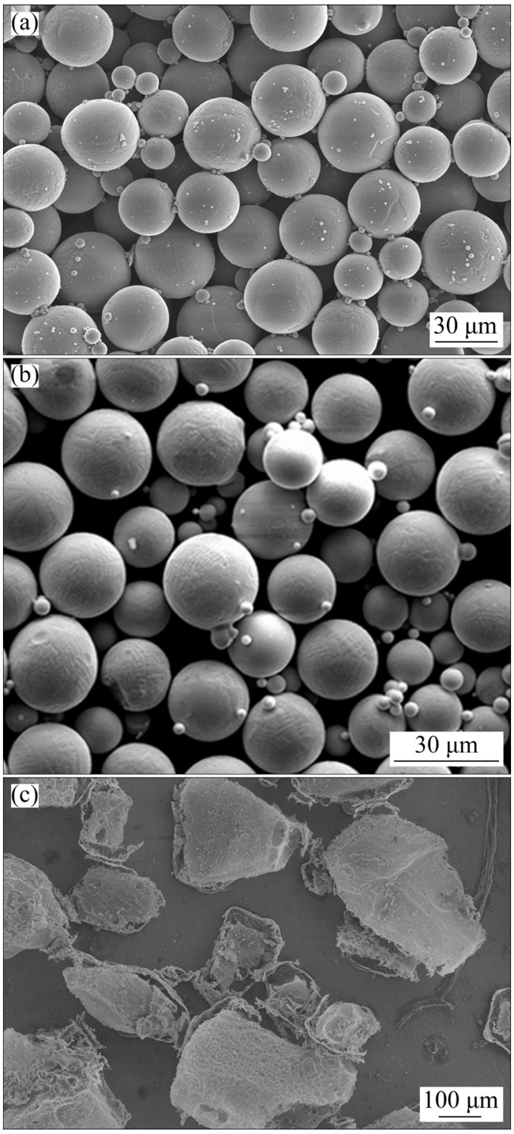

Fig. 1 SEM images of initial powders: (a) Ti6Al4V; (b) CoCrMo; (c) Ammonium bicarbonate (NH_4HCO_3 particles)

2.1.2 Green compacts

(1) Monolithic samples

Three different kinds of monolithic samples were fabricated, Ti6Al4V, Ti6Al4V/20CoCrMo composite and highly porous sample Ti6Al4V/30NH_4HCO_3. For fabricating the first sample, powders of Ti6Al4V were mixed with 1 wt.% polyvinyl alcohol (PVA), and then poured into an 8 mm-diameter stainless steel die and axially pressed at 300 MPa using an Instron universal testing machine (Model 1150). In order to fabricate the composite sample and the porous one, initially, the powders of Ti6Al4V were mixed with either CoCrMo or NH_4HCO_3 by using a Turbula mixer in dry conditions during 30 min, as illustrated in Fig. 2. For the composite and porous samples, a mixture of Ti6Al4V and 20 vol.% CoCrMo or 30 vol.% NH_4HCO_3, respectively, was used. Then, 1 wt.% of PVA was added to the mixture as a binder to give a higher green resistance to the sample. Next, the mixture was poured into an 8 mm-diameter stainless steel die and axially pressed at 300 MPa.

(2) Bilayer samples

Bilayer samples are composed of one layer of Ti6Al4V/20CoCrMo composite and another one of Ti6Al4V/30NH_4HCO_3, as shown in Fig. 2. First, each mixture of powders was independently obtained as above mentioned. Then, the mixture of Ti6Al4V/30NH_4HCO_3 was poured into the die and the surface was flattened by introducing the punch and slightly hand-pressed. Next, the mixture of Ti6Al4V/20CoCrMo was poured into the die. Finally, the sample was pressed at 300 MPa.

2.1.3 Consolidation step

Sintering of samples was used as a consolidation step. Before sintering, different steps were carried out depending on the sample characteristics. Samples containing space former particles were subjected to a thermal process to eliminate the salt particles at 180 °C during 6 h under high purity Ar in a horizontal furnace, see Fig. 2. Next, all samples were introduced into a horizontal furnace and heated at 500 °C, during 45 min, under high purity Ar with a heating rate of 10 °C/min in order to eliminate the PVA.

Then, the green samples were sintered in a Linseis L75V vertical dilatometer at 1130 °C with a

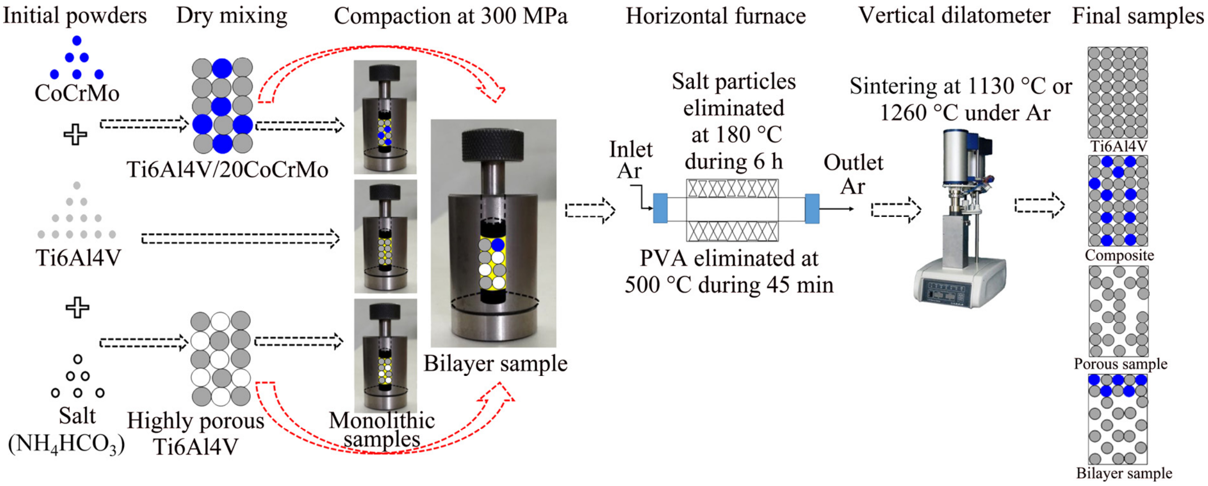

Fig. 2 Schematic diagram of fabrication process steps for monolithic and bilayer samples

dwell time of 5 min in Ar atmosphere. The heating rate varied during sintering; at temperatures between 50 and 1050 °C, a heating rate of 20 °C/min was used. Then, from 1050 °C up to the temperature of the sintering plateau, a heating rate of 5 °C/min was used. This was necessary to ensure that the temperature during the thermal cycle would stay close to the setup one, as the temperature of the furnace can increase by 10 or 20 °C with the inertia when higher heating rates are used.

In order to have a higher densification of the Ti6Al4V monolithic sample, this sample was sintered at 1260 °C with a 1 h plateau and a heating rate of 20 °C/min, as it was reported before [11,12]. This sample was used to compare the corrosion properties between the composite and the Ti6Al4V since the potentiodynamic tests are very sensitive to the porosity.

2.2 Sample characterization

2.2.1 Scanning electronic microscopy

After sintering, samples were cut and then, the surfaces were metallographically prepared for SEM observation by grinding/polishing with SiC abrasive papers and alumina suspensions (until 50 nm particle size). The microstructure of sintered samples was observed with a Tescan MIRA 3 LMU field emission scanning electron microscope (FE-SEM) coupled with an energy dispersive X-ray spectrometer (Bruker, XFlash 6/30) for elemental and mapping analysis.

2.2.2 Computed microtomography (CMT)

For more accurate analysis of the bilayer samples, 3D images were acquired by means of CMT, with a Zeiss Xradia 510 Versa 3D X-ray microscope. The beam intensity was set to be 120 kV, which was high enough to pass through Ti6Al4V/20CoCrMo composites and the porous layers with around 8 mm in diameter. 1600 projections were recorded around 360° of the sample with a CCD camera of 1024 × 1024 pixels. The resulting voxel size was around 8 μm. In addition, 3D images with lower pixel size (~2 μm) were acquired by cutting the samples in prisms of 2 mm × 2 mm × 4 mm. Such images were used to observe the distribution of the phases in the composite, as well as the interphase between the two layers. The 3D image analysis was performed by following the procedure described by OLMOS et al [19].

2.3 Permeability numerical simulations

Permeability was estimated by performing numerical simulations with the Absolute Permeability Experiment Simulation (APES) module in Avizo® software, which computes a scalar estimate of the permeability on the 3D binary images of the highly porous layer. APES implements the finite volume method to solve the Stokes equations for the velocity and pressure fields as explained elsewhere by MILLER et al [41]. Numerical simulations performed on Avizo are based on the Darcy law, in which a single phase incompressible newtonian fluid with a steady state laminar flow is assumed. The viscosity of the fluid passing throughout the pore media was selected to be 0.0045 Pa·s that represents the viscosity of the blood. It is necessary to establish the boundary conditions in the software that could be a pressure differential between the inner and the outer sides of the fluid, for this case, the inlet and outlet pressures were 130 and 100 kPa, respectively.

A minimum representative volume (MRV) was estimated by measuring the volume fraction of pores in 3D virtual cube cropped image. The initial cube had 20 voxels pre side and it was cropped from the middle of the 3D image to avoid the border effects. Then, a new cube was cropped increasing its size by 20 voxels per side. This operation was repeated until an almost constant pore volume fraction was attained. This process was also reported by OKUMA et al [42]. The smaller MRV that can give trusted results is a cube of 250 × 250 × 250 voxels. Thus, simulations were performed in cubes of 300 × 300 × 300 voxels (corresponding to around 14 mm^3), and in the three main directions of the cube, in which x and y represent the horizontal plane and z represents the vertical axis.

2.4 Compression tests

After sintering, the bottom and top surfaces of samples with 10 mm in height prepared for compression tests were polished and simple compression was performed following ASTM D695—02 with an Instron 1150 universal mechanical testing machine at a strain rate of 0.5 mm/min. The elastic modulus (E) and the yield strength (σ_y) were estimated from the stress−strain curves that were obtained from the load−displacement data provided by the machine. To calculate the stress, the surface area of the sample was corrected by assuming that the volume was constant during compression. The axial strain was calculated with the ratio of the real axial displacement (after machine stiffness correction) to the initial height of sample.

2.5 Corrosion tests

As a first step, the samples were immersed for 5 h in SBF under open circuit potential (OCP) conditions. After stabilization, potentiodynamic polarization (PD) tests were carried out for Ti6Al4V and Ti6Al4V/20CoCrMo samples. A typical configuration of three-electrode cell was used, where the sample functioned as working electrode, a high density graphite bar as counter electrode, and a saturate calomel electrode (SCE) as reference electrode. SBF with ion concentrations (mol/L) of 142.0 Na^+, 5 K^+, 2.5 Ca^{2+}, 1.5 Mg^{2+}, 147.8 Cl^-, 27.0 HCO_3^-; 1.0 HPO_4^{2-} and 0.5 SO_4^{2-} having a pH of 7.40 at 37 °C [43] was used. This electrolyte is nearly equal to the ion concentration of the human blood plasma. A Gamry Reference 600 potentiostat/galvanostat was used with a scanning rate of 2 mV/s in a potential range between −500 and 700 mV (vs SCE). Tafel extrapolations of the polarization curves were performed in order to determinate the corrosion potential (φ_{corr}) and the corrosion current density (J_{corr}) for the corrosion rate calculations.

3 Results and discussion

3.1 Sintering kinetics

The axial strain during the whole thermal cycle for monolithic and bilayer samples is shown in Fig. 3. At first, a dilation of all samples is observed, which is due to the thermal expansion of samples. Next, a shrinkage (negative axial strain) is noticed for all samples and it starts at almost the same temperature, around 660 °C, which indicates that sintering is activated. This temperature is consistent with that reported for the beginning of solid state sintering in Ti6Al4V powders [12,44]. After that, a continuous shrinkage occurs in all samples until the cooling stage is reached. For the Ti6Al4V/20CoCrMo sample, a change in the trend of the curve is seen at 1050 °C, which is associated to the beginning of the eutectic reaction of Ti and Co, as previously reported [28]. This reaction generates a

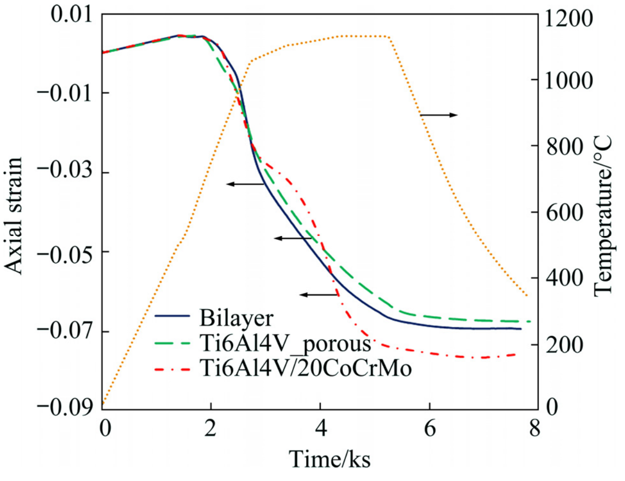

Fig. 3 Axial strain and temperature as function of time during whole sintering cycle

liquid phase that accelerates the axial strain when the viscosity of the liquid decreases as the temperature increases, finding the best condition for the liquid to spread at 1130 °C, as reported elsewhere [28]. The behavior of the bilayer sample is similar to that of the Ti6Al4V/30 NH_4HCO_3 sample. Although the layer of such sample is 3 times larger than that of the Ti6Al4V/ 20CoCrMo, the axial strain reached by the bilayer sample at the end of sintering is larger than that of the monolithic porous sample, indicating that Ti6Al4V/20CoCrMo layer contributes to the densification of the bilayer sample.

3.2 Microstructural characterization

Figure 4 shows the microstructures of monolithic samples of Ti6Al4V/30NH_4HCO_3 (Figs. 4(a) and (b)) and Ti6Al4V/20CoCrMo composite (Fig. 4(c)). Figures 4(d)−(f) show EDS elemental mappings of the composite. It is clearly seen that not only large pores are generated by the elimination of NH_4HCO_3 salt particles, but also small interparticle pores can be detected in Fig. 4(a). The spherical shape of raw Ti particles can be distinguished inside of the large pores in Fig. 4(b), which indicates that sintering is not well accomplished because of the low temperature used. On the other hand, the composite sample shows a biphasic microstructure with a few spherical pores (Fig. 4(c)). For this sample, the interparticle pores are no longer detected. With the aim to show the distribution of the phases in the composite sample, an EDS elemental mapping of the Ti6Al4V/ 20CoCrMo composite sample was performed, and the results are shown in Figs. 4(d)−(f). Three main different components of the composite sample were found: Ti6Al4V particles seen in the elemental analysis, CoCrMo particles detected as Co and

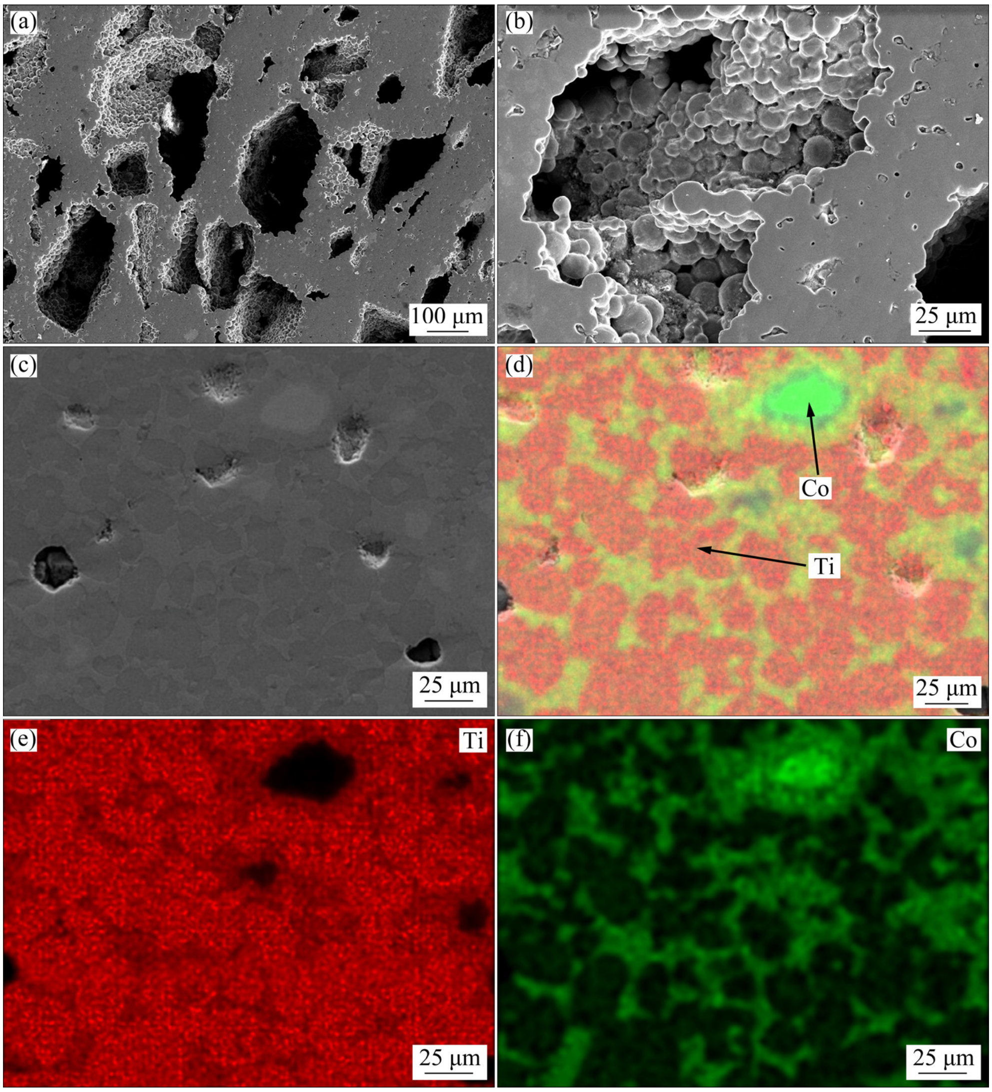

Fig. 4 SEM micrographs of Ti6Al4V/30NH_4HCO_3 (a, b), Ti6Al4V/20CoCrMo (c), and EDS elemental mappings (d−f)

Ti−Co phases formed by the eutectic reaction. It is clearly noticed that eutectic liquid fills the interparticle pores by surrounding the Ti6Al4V particles. The spherical pores could be formed either because of the space left by the dissolution of CoCrMo particles in the Ti6Al4V matrix, or by the surface tension of the liquid phase.

2D microstructure of the bilayer sample is shown in Fig. 5. The joint between the two layers seems to be good since no cracks are observed on the polished surface at the layers interface. The limits of both layers and the interface formed are indicated in Fig. 5(a). Small pores can be distinguished at the Ti6Al4V/20CoCrMo interface of the bilayer sample. Nevertheless, similar microstructure was observed for both samples, except for the darker dots located at the grain boundaries, as shown in Fig. 5(b). Those could be molybdenum precipitates but their origin is not clear. Thus, there is a transition zone between the composite and the porous layer with a different microstructure in Fig. 5(c). Finally, the bottom layer is composed of the highly porous Ti6Al4V with the same microstructure as observed in the monolithic sample, as shown in Fig. 5(d).

A 3D analysis of the microstructure of the bilayer sample was performed by images issued from CMT. For this purpose, 3D images were acquired with two different voxel sizes of 8 μm (Fig. 6(a)) and 2 μm (Fig. 6(b)). The image acquired with the higher voxel size allows to determine the macroscopical deformation and the distribution of large pores. Figure 6(a) shows a 2D virtual slice from the middle of the sample and measurements indicated that Ti6Al4V/20CoCrMo layer had a larger radial deformation (6.9%) in comparison to the Ti6Al4V/30NH_4HCO_3 layer (1%). This deformation was lower than the axial one obtained by dilatometry (Fig. 3) for the monolithic samples, which indicates a strong anisotropy in the macroscopic deformation. In addition, the transition between the two layers shows a progression in the radial deformation because of the stresses generated by the difference in densification of layers. In spite of the larger radial deformation undergone by the upper layer

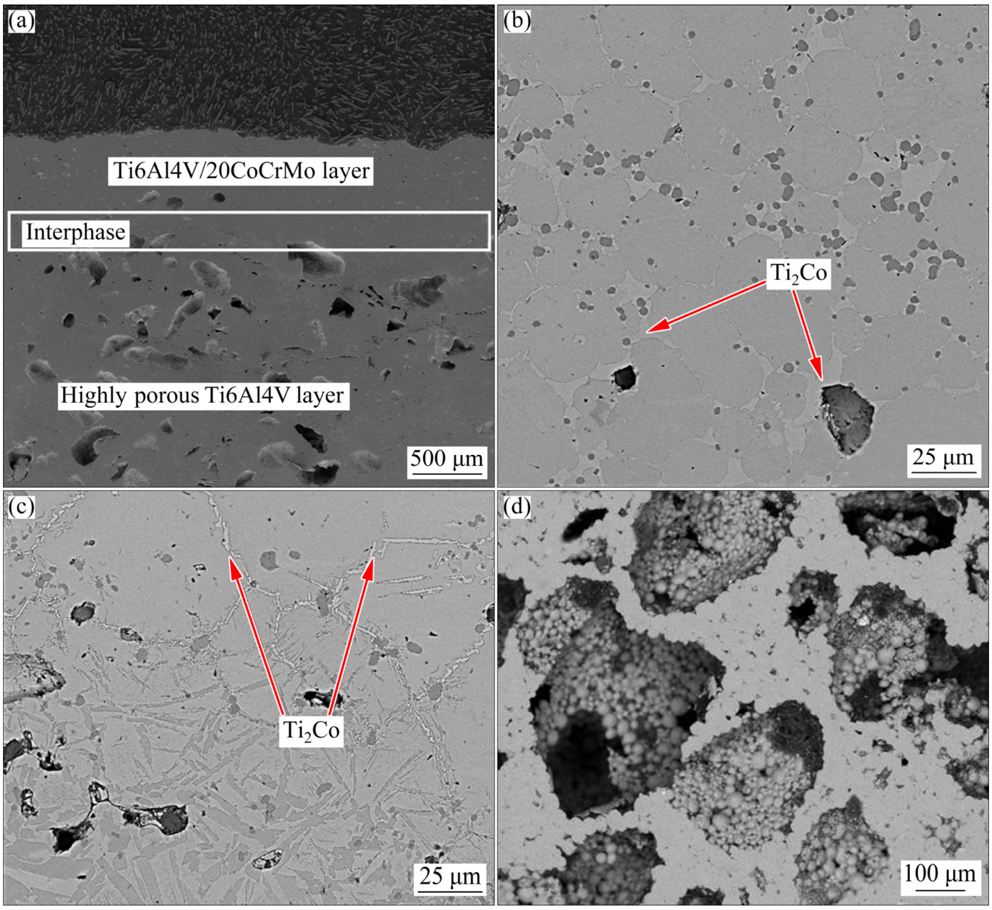

Fig. 5 SEM micrographs of bilayer sample sintered at 1130 °C: (a) Whole sample; (b) Ti6Al4V/20CoCrMo layer; (c) Interphase zone; (d) Ti6Al4V/30NH_4HCO_3 layer

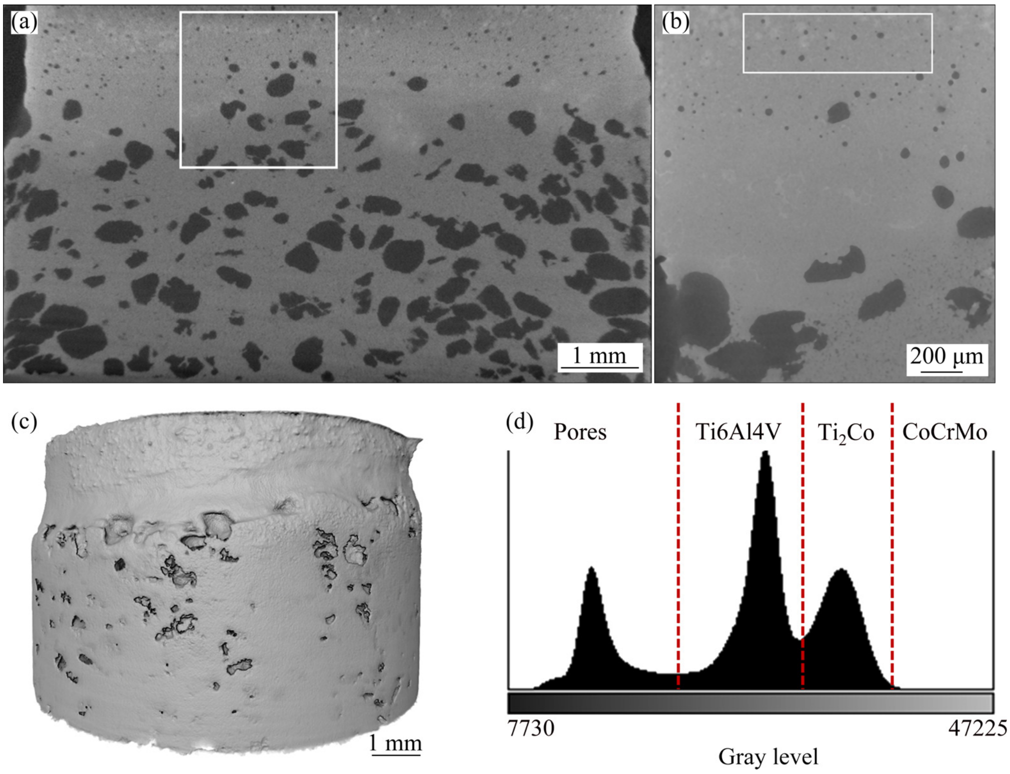

Fig. 6 2D virtual slices of bilayer sample at different voxel size resolutions of 8 μm (a) and 2 μm (b), 3D rendering of whole sample (c) and grey level histogram of complete 3D image (d)

(around 7 times), no cracks are formed in the sample, which is mainly attributed to the formation of necks between Ti6Al4V particles during the solid state sintering achieved before the eutectic liquid appears and densifies the Ti6Al4V/20CoCrMo layer. A 3D rendering of the bilayer sample is shown in Fig. 6(c) and it is clearly observed that larger shrinkage is obtained in the top layer, which corresponds to the Ti6Al4V/ 20CoCrMo layer. It seems that the eutectic liquid probably drains out of the sample, although in the 2D virtual slices of the whole sample, no segregation of the Ti_2Co phase is found.

Figure 6(b) shows a 2D virtual slice of the 3D image acquired with smaller voxel size, and this image was taken at the interphase of both layers with the aim of observing the distribution of different phases in the Ti6Al4V/20CoCrMo layer and the transition between the two layers, as indicated in the white square of Fig. 6(a). Three different gray levels are discernible in the image, black, light grey and dark grey, which correspond to materials with different atomic masses. Small and circular pores are found in the top layer and a transition zone with larger isolated pores is also distinguished. Finally, the lower part of Fig. 6(b) shows the bottom layer, which is formed by the largest pores and small interparticle pores that can barely be noticed. The grey level histogram of the whole 3D image (Fig. 6(d)) indicates three main peaks, , which confirms the qualitative observations above mentioned. The lower grey level indicates the pores, then, the second peak corresponds to the Ti6Al4V phase that has the lower atomic mass. The third one shows a higher grey level and it is associated to the Ti_2Co phase, which is the eutectic liquid distributed among the Ti6Al4V particles. Besides the three main peaks, a small quantity of voxels are detected with higher grey level are detected, which indicates the presence of material with a higher atomic mass, which is the remaining CoCrMo particles, as indicated in Fig. 6(d).

In order to obtain information of each phase of the whole sample, an image treatment procedure was followed. First, the images are filtered with a median filter in the Image J software. Then, the segmentation is achieved by selecting the grey level that corresponds to each phase, as indicated in Fig. 6(d). Qualitative data of the Ti6Al4V/ 20CoCrMo layer are obtained from the white rectangle shown in Fig. 6(b). After segmentation, a 3D rendering of the four different phases that form in the top layer is shown in Fig. 7. The distribution of the Ti6Al4V phase is observed in Fig. 7(a), meanwhile, the Ti_2Co phase is shown in Fig. 7(b). In both cases, each phase is completely interconnected. This means that the Ti_2Co phase is well distributed into the interparticle pores. The volume fractions of Ti6Al4V, Ti_2Co, CoCrMo and pores estimated from the 3D images are 74.1%, 24.02%, 0.08% and 1.8%, respectively, see Table 1. It is found that most of the small CoCrMo particles diffuse into the eutectic reaction, whereas the remaining small pieces of CoCrMo particles are shown in Fig. 7(c). The densification of the Ti6Al4V/20CoCrMo layer is well developed since only 1.8% of remaining pores after sintering are found, which indicates that the eutectic liquid helps to densify the sample. Figure 7(d) shows the distribution of the remaining pores in the Ti6Al4V/20CoCrMo layer after sintering, and as it is anticipated by SEM observations, spherical and isolated pores are found. The pore size distribution is plotted in Fig. 8, in which larger pores can attain 45 µm, and the median size pores reach 20 µm.

The pore size distribution of the bilayer sample was separated by layer since each one has different characteristics (see Fig. 8). The pores found in the Ti6Al4V/30NH_4HCO_3 are mainly obtained from the addition of the NH_4HCO_3 salt particles, which means that pores higher than 100 µm were generated by eliminating NH_4HCO_3 salt particles, contrary to this, smaller pores are due to the initial packing and small densification is as a result of the low sintering temperature used. From Fig. 8, it is estimated that 86% of the total pores are larger than 100 µm, which represents around 27.5 vol.% of the total porosity of the porous layer (see Table 1). This is consistent with the volume fraction of the NH_4HCO_3 salt particles added during the fabrication step. This confirms that it is possible to control the quantity of pores and size by the space holder method. The median size found was 207 µm, which is over 10 times as large as the median size

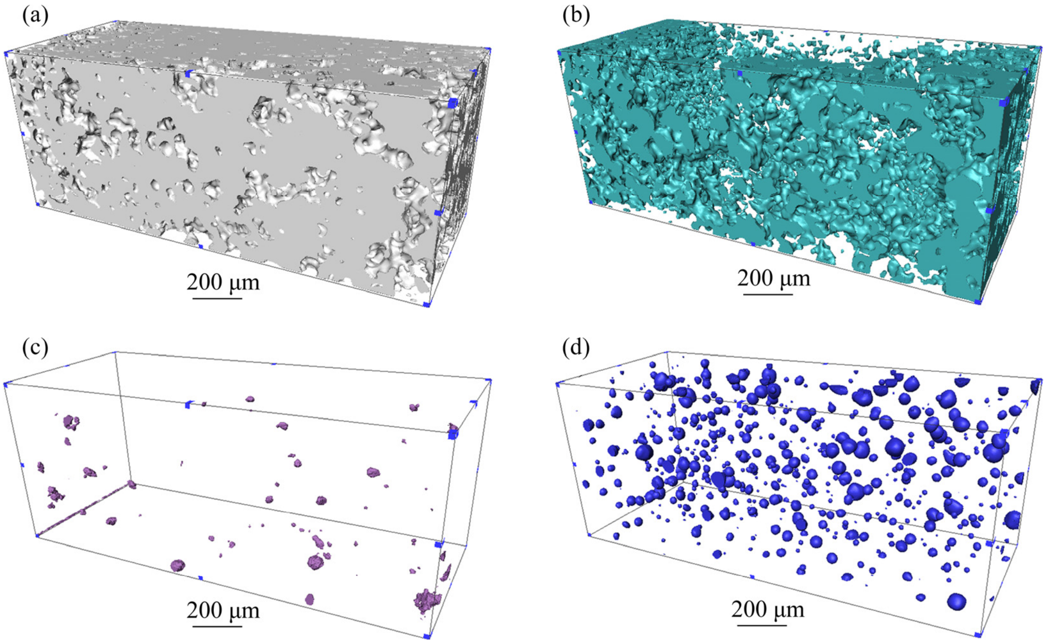

Fig. 7 3D rendering of four different phases in Ti6Al4V/20CoCrMo layer after sintering: (a) Ti6Al4V; (b) Ti_2Co; (c) CoCrMo; (d) Pores

Table 1 Quantitative data measured from 3D images

Layer	Volume fraction/%			
	Ti6Al4V	Ti_2Co	CoCrMo	Pores
Ti6Al4V/20CoCrMo	74	24	0.08	1.8
Ti6Al4V/30NH_4HCO_3	68	−	−	32

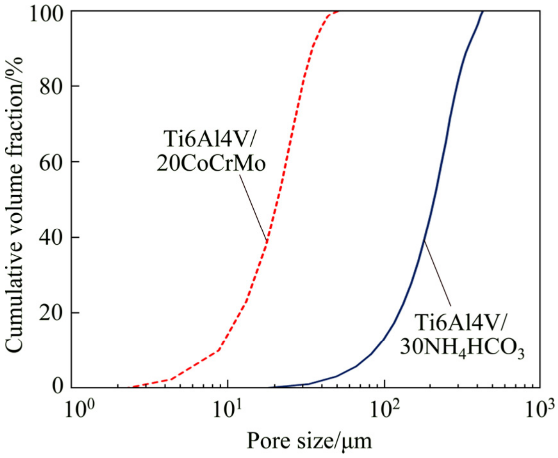

Fig. 8 Pore size distribution in Ti6Al4V/20CoCrMo and Ti6Al4V/$30NH_4HCO_3$

measured in the Ti6Al4V/20CoCrMo sample. ZHENG et al [45] demonstrated that the formation of bone tissue is favored by a pore size distribution ranging between 50 and 300 μm, which is very close to that obtained in the porous layer of this work.

The pore connectivity in both layers was assessed as described by OLMOS et al [19] and it is found that porous layer shows a 90% pore connectivity. In Fig. 9(b), a 3D rendering of pores is shown, in which the pseudo colors illustrate the connectivity among them. On the other hand, the Ti6Al4V/20CoCrMo layer has null connectivity, as it can be seen in Fig. 7(d). This indicates that pores are not connected between layers, which is important since pores can strongly reduce the wear and corrosion resistance of materials.

3.3 Permeability analysis

Permeability in the Ti6Al4V/$30NH_4HCO_3$ layer was estimated from numerical simulations in both directions of the sample, vertical and radial, shown in Fig. 9(a). The values are listed in Table 2, and the vertical direction shows lower values, around the half of the radial direction. The permeability values are in the lower range of those experimentally measured by NAUMAN et al [16] in human vertebral and proximal femur bones, who reported a large range of permeability values for human bones (2×10^{-8} to 2.68×10^{-11} m^2). They also measured larger values of permeability in the radial direction pointing out a high anisotropy when

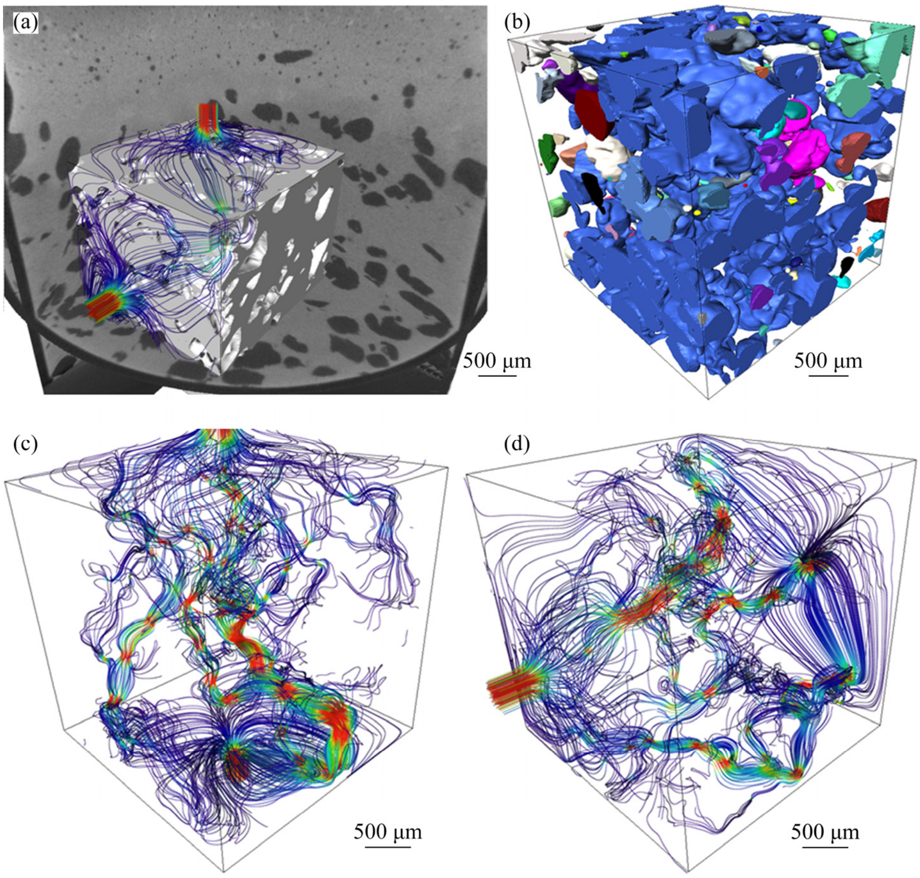

Fig. 9 2D orthoslices and 3D volume rendering of Ti6Al4V/$30NH_4HCO_3$ layer (a), 3D rendering of pores (b) and streamlines for flow of blood through pores in vertical (c) and radial (d) directions

Table 2 Quantitative data of pores of bilayer sample, calculated from 3D images

Layer	Median pore size/μm	Permeability in radial axis/m^2	Permeability in vertical axis/m^2	Tortuosity
Ti6Al4V/20CoCrMo	20	–	–	–
Ti6Al4V/30NH_4HCO_3	207	6.08×10^{-11}	2.97×10^{-11}	1.9

permeability was measured in the longitudinal and transversal directions of bones, of which the axial/radial permeability ratio goes from 2.05 to 23.3. They concluded that anisotropy is relative to the anatomic site of the bone. The values of permeability obtained for the porous layer are lower than those reported for the human trabecular bone ($(0.4-11)\times10^{-9}$ m^2) measured from fresh-frozen calcanea of cadavers by GRIMM and WILLIAMS [15]. On the other hand, permeability values are consistent with those experimentally measured for porous materials with the similar pore volume fraction and pore sizes fabricated by either space holder [17] or additive manufacturing [46,47]. Figures 9(c) and (d) show the simulated flow patterns through the Ti6Al4V/30NH_4HCO_3 layer, which has a pore volume fraction of 32%. Four main channels allow the fluid throughout the samples in the vertical direction (see Fig. 9(c)), showing an increase in the velocity of the fluid in different zones that are identified by the red colors in the paths. For the radial direction, Fig. 9(d), six main channels can be distinguished, increasing the paths by the fluid throughout the sample, although an increase in the velocity is also noticed, the color map indicates lower velocities in such direction, which helps to improve the permeability in the radial direction.

3.4 Mechanical behavior

The stress−strain curves under compression of the monolithic and bilayer samples are shown in Fig. 10. It is clear that Ti6Al4V/20CoCrMo is much stronger that Ti6Al4V/30NH_4HCO_3, as expected. It can also be observed that Ti6Al4V/20CoCrMo sample shows lower plastic deformation, as it can be confirmed from the picture of the sample after compression, which shows a fracture in the radial direction. On the other hand, the porous sample is plastically deformed by closing the large pores with no fracture visible, as it can be noticed from the image of the sample after compression tests. The bilayer sample shows a similar slope at the beginning compared with the Ti6Al4V/20CoCrMo monolithic sample, but when the stress reaches 60 MPa the bilayer sample presents a continuous plastic deformation, which suggests that large pores in the Ti6Al4V/30NH_4HCO_3 layer undergo deformation. The increment on the stress may be due to the resistance of the Ti6Al4V/20CoCrMo layer until the maximum stress reaches, then the bilayer fails. From the image after compression of the bilayer sample it is deduced that the porous layer is plastically deformed and some fractures are formed in the vertical direction of the sample, which seems to be originated at the interphase with the Ti6Al4V/20CoCrMo layer. This could be an indicative of stress generated at the interphase of the porous sample. However, a deep investigation of the fracture behavior should be addressed to confirm the effect of each layer on the compression behavior.

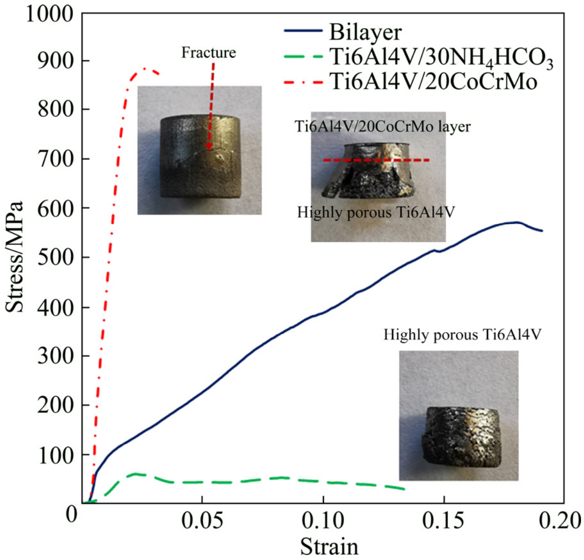

Fig. 10 Stress–strain curves of compression tests for samples after sintering

The elastic modulus, E, is defined as the average slope of the initial linear section of the stress−strain curve. The yield stress, σ_y, is the stress value at the end of this section. E and σ_y for the monolithic and bilayer samples are listed in Table 3. The value of E for the bilayer sample increases by 4 times with respect to that of the monolithic

Table 3 Mechanical and corrosion properties of monolithic and bilayer samples

Sample	E/GPa	σ_y/MPa	φ_{corr}/V	J_{corr}/(A·cm^{-2})	Corrosion rate/(m·a^{-1})
Ti6Al4V/20CoCrMo	60	610	−0.1	3.15×10^{-9}	4.952×10^{-4}
Ti6Al4V/30NH$_4$HCO$_3$	4	52	−	−	−
Bilayer	20	64	−	−	−
Ti6Al4V	85	800	−0.1319	2.52×10^{-7}	3.712×10^{-2}

The unit “m/a” of corrosion rate represents “m/year”

Ti6Al4V/30NH$_4$HCO$_3$. On the contrary, the σ_y undergoes a smaller increment (only 23% increment i.e., 1.23 times of the initial value). This indicates that the stiffness of the sample is affected by the Ti6Al4V/20CoCrMo layer more obviously, although the mechanical strength during the plastic deformation is highly increased with respect to the monolithic Ti6Al4V/30NH$_4$HCO$_3$ sample. The E value (4 GPa) of the porous sample Ti6Al4V/30NH$_4$HCO$_3$ is similar to that reported by LI et al [48] for porous Ti with similar volume fraction of pores. Nevertheless, the compressive strength reported by LI et al [48] is 3 times higher than the one obtained here, which is mainly due to the sintering temperature used (1300 °C) that promotes the development of interparticle necks. In general view, the values of E and σ_y obtained for the bilayer sample are still in the range of those of human bones (E=0.06−20 GPa and σ_y=5−200 MPa) reported by WANG et al [6].

3.5 Corrosion resistance

Potentiodynamic polarization curves of sintered monolithic samples of Ti6Al4V and Ti6Al4V/20CoCrMo in SBF are shown in Fig. 11. The Ti6Al4V sample was used in this study as a comparison parameter, for such case, this sample was sintered at 1260 °C in order to obtain a higher relative density of 96%. The corrosion potential (φ_{corr}) and the corrosion current density (J_{corr}) of both materials, were estimated by using the Tafel analysis and the results are listed in Table 3. The addition of CoCrMo to a bilayer configuration sample, as the one proposed in this investigation, resulted in a slight increment of the φ_{corr} value from −0.1319 to −0.1 V, meaning a less tendency to corrosion. Both values are higher than those reported by YANG et al [49] for Ti6Al4V samples prepared by selective electron beam melting.

The addition of 20 vol.% of CoCrMo to the Ti6Al4V matrix decreased the J_{corr} values obtained for the Ti6Al4V from 2.52×10^{-7} to 3.15×10^{-9} A/cm^2, which means a reduction of about two orders of magnitude of the J_{corr} values. It is worth mentioning that a decrease in J_{corr} is closely linked to a decrement in the corrosion rate, denoting a better corrosion performance of the Ti6Al4V/20CoCrMo sample. Also, passivation is clearly seen at ~0.2 V in the anodic region. After this value, passivation continues to a value close to 1 V at which passivation film seems to fail, and a moderate dissolution region is shown. Calculations of the corrosion rates by using the Faraday’s law [50] indicated that the corrosion rate could be decreased by two orders (see Table 3) as a result of the eutectic phase Ti$_2$Co homogeneously distributed in the sample. Besides, the behavior of the curve during the anodic reaction of the Ti6Al4V/20CoCrMo sample shows a better stabilization than the Ti6Al4V sample, which indicates that pitting is not present in the former sample.

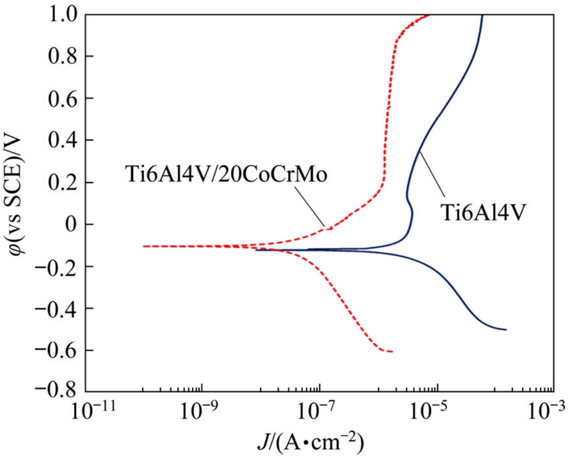

Fig. 11 Polarization potentiodynamic curves of Ti6Al4V and Ti6Al4V/20CoCrMo samples

4 Conclusions

(1) The fabrication of bilayer components without cracks or any separation of layers was attained. An important role in this success is played

by the fact that, while densification behavior of the bilayer is similar to that of the monolithic layers. A minor effect of the interface is noticed as the matrix in both layers is Ti6Al4V. A well-established gradual change in the microstructure from the Ti6Al4V/20CoCrMo layer to the Ti6Al4V/ $30NH_4HCO_3$ layer is obtained and the distribution of all phases that compound the bilayer sample is obtained due to the chosen processing technique. Pore size distribution and permeability values, as well as E and σ_y, are in the range of those reported for the human bones. The corrosion resistance of the Ti6Al4V/20CoCrMo is better than that of the Ti6Al4V in a simulated body fluid, demonstrating a decrease in corrosion rate and better stabilization of the anodic reaction.

(2) The novel bilayer material designed can potentially benefit the production of implants with high corrosion resistance and low elastic modulus, with permeability similar to that of human bones. Customized implants with improved wear performance and increase in vivo lifetime, compared with monolithic materials like CoCrMo and Ti6Al4V as the most popular commercial biomedical alloys, can be achieved.

Acknowledgments

This work was supported by the National Council for Science and Technology CONACYT (Mihalcea PhD scholarship 473734 and Dr. Chávez postdoctoral fellow 000614). The authors would like to thank the CIC of the UMSNH and the National Laboratory SEDEAM-CONACYT for the financial support and the facilities provided for the development of this study. We would also like to thank the Laboratory "LUMIR" Geosciences of the UNAM, Juriquilla, for the 3D image acquisition and processing.

References

[1] TEOH S H. Engineering materials for biomedical applications (Vol. 1) [M]. London: World Scientific, 2004.

[2] DEWIDAR M M, KHALIL K A, LIM J K. Processing and mechanical properties of porous 316L stainless steel for biomedical applications [J]. Transactions of Nonferrous Metals Society of China, 2007, 17(3): 468−473.

[3] DOURANDISH M, GODLINSKI D, SIMCHI A, FIROUZDOR V. Sintering of biocompatible P/M Co–Cr–Mo alloy (F-75) for fabrication of porosity-graded composite structures [J]. Materials Science and Engineering A, 2008, 472(1−2): 338−346.

[4] NIINOMI M, NAKAI M. Titanium-based biomaterials for preventing stress shielding between implant devices and bone [J]. International Journal of Biomaterials, 2011, 2011: 836587.

[5] BAHRAMINASAB M, SAHARI B B, EDWARDS K L, FARAHMAND F, ARUMUGAM M, HONG T S. Aseptic loosening of femoral components—A review of current and future trends in materials used [J]. Materials and Design, 2012, 42: 459−470.

[6] WANG X J, XU S Q, ZHOU S W, XU W, LEARY M, CHOONG P, QIAN M, BRANDT M, XIE M Y. Topological design and additive manufacturing of porous metals for bone scaffolds and orthopaedic implants: A review [J]. Biomaterials, 2016, 83: 127−141.

[7] TORRES Y, RODRÍGUEZ J A, ARIAS S, ECHEVERRY M, ROBLEDO S, AMIGO V, PAVÓN J J. Processing, characterization and biological testing of porous titanium obtained by space-holder technique [J]. Journal of Materials Science, 2012, 47(18): 6565−6576.

[8] REIG L, AMIGÓ V, BUSQUETS D J, CALERO J A. Development of porous Ti6Al4V samples by microsphere sintering [J]. Journal of Materials Processing Technology, 2012, 212(1): 3−7.

[9] KALANTARI S M, ARABI H, MIRDAMADI S, MIRSALEHI S A. Biocompatibility and compressive properties of Ti−6Al−4V scaffolds having Mg element [J]. Journal of the Mechanical Behavior of Biomedical Materials, 2015, 48: 183−191.

[10] TORRES Y, LASCANO S, BRIS J, PAVÓN J, RODRIGUEZ J A. Development of porous titanium for biomedical applications: A comparison between loose sintering and space-holder techniques [J]. Materials Science and Engineering C, 2014, 37: 148−155.

[11] CABEZAS-VILLA J L, LEMUS-RUIZ J, BOUVARD D, JIMÉNEZ O, VERGARA-HERNÁNDEZ H J, OLMOS L. Sintering study of Ti6Al4V powders with different particle sizes and their mechanical properties [J]. International Journal of Minerals, Metallurgy and Materials, 2018, 25(12): 1389−1401.

[12] CABEZAS-VILLA J L, OLMOS L, BOUVARD D, LEMUS-RUIZ J, JIMÉNEZ O. Processing and properties of highly porous Ti6Al4V mimicking human bones [J]. Journal of Materials Research, 2018, 33(6): 650−661.

[13] WANG X H, LI J S, HU R, KOU H C, ZHOU L. Mechanical properties of porous titanium with different distributions of pore size [J]. Transactions of Nonferrous Metals Society of China, 2013, 23(8): 2317−2322.

[14] TRUEBA P, CHICARDI E, RODRÍGUEZ-ORTIZ J A, TORRES Y. Development and implementation of a sequential compaction device to obtain radial graded porosity cylinders [J]. Journal of Manufacturing Processes, 2020, 50: 142−153.

[15] GRIMM M, WILLIAMS J. Measurements of permeability in human calcaneal trabecular bone [J]. Journal of Biomechanics, 1997, 30(7): 743−745.

[16] NAUMAN E, FONG K, KEAVENY T. Dependence of intertrabecular permeability on flow direction and anatomic site [J]. Annals of Biomedical Engineering, 1999, 27: 517−524.

[17] SINGH R, LEE P D, LINDLEY T C, DASHWOOD R J, FERRIE E, IMWINKELRIED T. Characterization of the structure and permeability of titanium foams for spinal fusion devices [J]. Acta Biomaterialia, 2009, 5: 477−487.

[18] VARLEY M C, NEELAKANTAN S, CLYNE T W, DEAN J, BROOKS R A, MARKAKI A E. Cell structure, stiffness and permeability of freeze-dried collagen scaffolds in dry and hydrated states [J]. Acta Biomaterialia, 2016, 33: 166−175.

[19] OLMOS L, BOUVARD D, CABEZAS-VILLA J L, LEMUS-RUIZ J, JIMÉNEZ O, ARTEAGA D. Analysis of compression and permeability behavior of porous Ti6Al4V by computed microtomography [J]. Metals and Materials International, 2018, 25(3): 669−682.

[20] ITÄLÄ A I, YLÄNEN H O, EKHOLM C, KARLSSON K H, ARO H T. Pore diameter of more than 100 μm is not requisite for bone ingrowth in rabbits [J]. Journal of Biomedical Materials Research Part A, 2001, 58: 679−683.

[21] BRAEM V, CHAUDHARI A, VIVAN CARDOSO M, SCHROOTEN J, DUYCK J, VLEUGELS J. Peri- and intra-implant bone response to microporous Ti coatings with surface modification [J]. Acta Biomaterialia 2014, 10(2): 986−995.

[22] LOH Q L, CHOONG C. Three-dimensional scaffolds for tissue engineering applications: Role of porosity and pore size [J]. Tissue Engineering Part B: Reviews, 2013, 19(6): 485−502.

[23] KRASICKA-CYDZIK E, OKSIUTA Z, DABROWSKI J R. Corrosion testing of sintered samples made of the Co−Cr−Mo alloy for surgical applications [J]. Journal of Materials Science: Materials in Medicine, 2005, 16(3): 197−202.

[24] VARANO R, BOBYN J D, MEDLEY J B, YUE S. Effect of microstructure on the dry sliding friction behavior of CoCrMo alloys used in metal-on-metal hip implants [J]. Journal of Biomedical Materials Research Part B: Applied Biomaterials, 2006, 76(2): 281−286.

[25] SONG C B, PARK H B, SEONG H G, LOPEZ H F. Development of athermal ε-martensite in atomized Co−Cr−Mo−C implant alloy powders [J]. Acta Biomaterialia, 2006, 2(6): 685−691.

[26] WANG R, WELSCH G. Evaluation of an experimental Ti−Co alloy for dental restorations [J]. Journal of Biomedical Materials Research Part B: Applied Biomaterials, 2013, 101: 1419−1427.

[27] MUTLU I. Synthesis and characterization of Ti−Co alloy foam for biomedical applications [J]. Transactions of Nonferrous Metals Society of China, 2016, 26(1): 126−137.

[28] MIHALCEA E, VERGARA-HERNÁNDEZ H J, OLMOS L, JIMENEZ O. Semi-solid sintering of Ti6Al4V/CoCrMo composites for biomedical applications [J]. Materials Research, 2019, 22: e20180391.

[29] CHO M, HONG E, SO J, SONG S, KIM B S, YAMAMOTO A, KIM Y S, CHO J, CHOE H. Tribological properties of biocompatible Ti−10W and Ti−7.5TiC−7.5W [J]. Journal of the Mechanical Behavior of Biomedical Materials, 2014, 30: 214−222.

[30] LIEBERMAN S I, GOKHALE A M, TAMIRI-SAKANDALA S, BHAT R B. Three-dimensional microstructural characterization of discontinuously reinforced Ti64−TiB composites produced via blended elemental powder metallurgy [J]. Materials Characterization, 2009, 60(9): 957−963.

[31] SELVA KUMAR M, CHANDRASEKAR P, CHANDRAMOHAN P, MOHANRAJC M. Characterisation of titanium–titanium boride composites processed by powder metallurgy techniques [J]. Materials Characterization, 2012, 73: 43−51.

[32] SOBCZAK J J, DRENCHEV L. Metallic functionally graded materials: a specific class of advanced composites [J]. Journal of Materials Science and Technology, 2013, 29(4): 297−316.

[33] BONIECKI M, KALINSKI D, LIBRANT Z, WESOLOWSKI W. Superplastic joining of alumina and zirconia ceramics [J]. Journal of the European Ceramic Society, 2007, 27(2−3): 1351−1355.

[34] KIEBACK B, NEUBRAND A, RIEDEL H. Processing techniques for functionally graded materials [J]. Materials Science and Engineering A, 2003, 362(1−2): 81−106.

[35] BENDER S, CHALIVENDRA V, RAHBAR N, EL WAKIL S. Mechanical characterization and modeling of graded porous stainless steel specimens for possible bone implant applications [J]. International Journal of Engineering Science, 2012, 53: 67−73.

[36] DEWIDAR M M, LIM J K. Properties of solid core and porous surface Ti−6Al−4V implants manufactured by powder metallurgy [J]. Journal of Alloys and Compounds, 2008, 454(1−2): 442−446.

[37] LEE J H, PARK H J, HONG S H, KIM J T, LEE W H, PARK J M, KIM K B. Characterization and deformation behavior of Ti hybrid compacts with solid-to-porous gradient structure [J]. Materials and Design, 2014, 60: 66−71.

[38] AHMADI S, SADRNEZHAAD S K. A novel method for production of foamy core@ compact shell Ti6Al4V bone-like composite [J]. Journal of Alloys and Compounds, 2016, 656: 416−422.

[39] CHÁVEZ J, OLMOS L, JIMÉNEZ O, BOUVARD D, RODRÍGUEZ E, FLORES M. Sintering behaviour and mechanical characterisation of Ti64/xTiN composites and bilayer components [J]. Powder Metallurgy, 2017, 60(4): 257−266.

[40] CHÁVEZ J, ALEMÁN O J, MARTÍNEZ M F, VERGARA-HERNÁNDEZ H J, OLMOS L, GARNICA-GONZÁLEZ P, BOUVARD D. Characterization of Ti6Al4V–Ti6Al4V/30Ta bilayer components processed by powder metallurgy for biomedical applications [J]. Metals and Materials International, 2020, 26(2): 205−220.

[41] MILLER K J, ZHU W L, MONTESI L G, GAETANI G A. Experimental quantification of permeability of partially molten mantle rock [J]. Earth and Planetary Science Letters, 2014, 388: 273−282.

[42] OKUMA G, KADOWAKI D, SHINODA Y, AKATSU T, GUILLON O, WAKAI F. Determination of the size of representative volume element for viscous sintering [J]. Journal of the Ceramic Society of Japan, 2016, 124(4): 421−425.

[43] KOKUBO T, TAKADAMA H. How useful is SBF in

predicting in vivo bone bioactivity? [J]. Biomaterials, 2006, 27(15): 2907−2915.

[44] XU X, NASH P. Sintering mechanisms of Armstrong prealloyed Ti−6Al−4V powders [J]. Materials Science and Engineering A, 2014, 607: 409−416.

[45] ZHENG J P, CHEN L J, CHEN D Y, SHAO C S, YI M F, ZHANG B. Effects of pore size and porosity of surface-modified porous titanium implants on bone tissue ingrowth [J]. Transactions of Nonferrous Metals Society of China, 2019, 29(12): 2534−2545.

[46] ZHANG Z, JONES D, YUE S, LEE P D, JONES J R, SUTCLIFFE C J, JONES E. Hierarchical tailoring of strut architecture to control permeability of additive manufactured titanium implants [J]. Materials Science and Engineering C, 2013, 33(7): 4055−4062.

[47] DIAS M R, FERNANDES P R, GUEDES J M, HOLLISTER S J. Permeability analysis of scaffolds for bone tissue engineering [J]. Journal of Biomechanics, 2012, 45(6): 938−944.

[48] LI B Q, LI Z Q, LU X. Effect of sintering processing on property of porous Ti using space holder technique [J]. Transactions of Nonferrous Metals Society of China, 2015, 25(9): 2965−2973.

[49] YANG X, WANG W L, MA W J, WANG Y, YANG J G, LIU S F, TANG H P. Corrosion and wear properties of micro-arc oxidation treated Ti6Al4V alloy prepared by selective electron beam melting [J]. Transactions of Nonferrous Metals Society of China, 2020, 30(8): 2132−2142.

[50] BURNAT B, WALKOWIAK-PRZYBYŁO M, BŁASZCZYK T, KLIMEK L. Corrosion behaviour of polished and sandblasted titanium alloys in PBS solution [J]. Acta of Bioengineering and Biomechanics, 2013, 15: 87−94.

粉末冶金法制备 Ti6Al4V/20CoCrMo 与多孔 Ti6Al4V 双层生物医用材料的设计与表征

E. MIHALCEA[1], H. J. VERGARA-HERNÁNDEZ[1], O. JIMENEZ[2], L. OLMOS[3], J. CHÁVEZ[4], D. ARTEAGA[5]

1. División de Estudios de Posgrado e Investigación, Tecnológico Nacional de México/ITMorelia,
Av. Tecnológico # 1500, Colonia Lomas de Santiaguito, Morelia, C.P. 58120, México;
2. Universidad de Guadalajara, DIP, José Guadalupe Zuno # 48, Los Belenes, Zapopan, C. P. 45100, México;
3. INICIT, Universidad Michoacana de San Nicolás de Hidalgo, Fco. J. Mujica S/N, Morelia, C. P. 58060, México;
4. Departamento de Ingeniería Mecánica Eléctrica, CUCEI, Universidad de Guadalajara,
Blvd. Marcelino García Barragán 1421, Olímpica, C. P. 44430 Guadalajara, Jalisco, México;
5. Centro de Geociencias, Universidad Nacional Autónoma de México,
Blvd. Juriquilla No. 3001, Querétaro 76230, México

摘　要：制备 Ti6Al4V/20CoCrMo 与多孔 Ti6Al4V 生物医用双层复合材料。采用传统粉末冶金技术，以半固态烧结为固结步骤，制备具有致密 Ti6Al4V/20CoCrMo 表层和多孔 Ti6Al4V 底层的双层样品，以更好地模拟天然骨。采用膨胀法研究双层试样的致密化行为，通过扫描电镜(SEM)和显微计算机断层成像 (CMT)观察其显微组织，并分别通过压缩试验和动电位试验评价其力学性能和耐腐蚀性能。结果表明，在界面对致密化无负面影响的情况下，可得到无裂纹的双层样品。多孔层的渗透率值在较低的人体骨骼的渗透率范围内。样品的压缩特性由 Ti6Al4V 多孔层决定。此外，Ti6Al4V/20CoCrMo 的耐腐蚀性能优于 Ti6Al4V 的耐腐蚀性能，提高双层样品的耐腐蚀性。研究粉末冶金法制备具有致密 Ti6Al4V/20CoCrMo 表层和多孔 Ti6Al4V 底层的双层结构材料，有助于生产定制化、具有良好磨损性能和体内寿命的植入物。

关键词：双层结构；复合材料；孔隙率；烧结；渗透率；压缩行为；腐蚀

(Edited by Wei-ping CHEN)